

Article

## Snapshotting the Excited-State Planarization of Chemically-Locked *N,N*-Disubstituted-dihydrodibenzo[*a,c*]phenazines

Wei Chen, Chi-Lin Chen, Zhiyun Zhang, Yi-An Chen, Wei-Chih Chao, Jianhua Su, He Tian, and Pi-Tai Chou

*J. Am. Chem. Soc.*, **Just Accepted Manuscript** • DOI: 10.1021/jacs.6b11789 • Publication Date (Web): 10 Jan 2017

Downloaded from <http://pubs.acs.org> on January 10, 2017

### Just Accepted

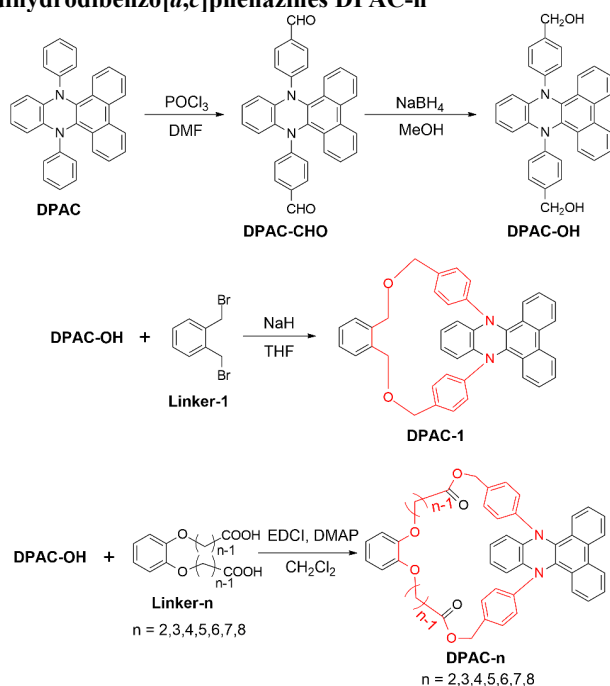
“Just Accepted” manuscripts have been peer-reviewed and accepted for publication. They are posted online prior to technical editing, formatting for publication and author proofing. The American Chemical Society provides “Just Accepted” as a free service to the research community to expedite the dissemination of scientific material as soon as possible after acceptance. “Just Accepted” manuscripts appear in full in PDF format accompanied by an HTML abstract. “Just Accepted” manuscripts have been fully peer reviewed, but should not be considered the official version of record. They are accessible to all readers and citable by the Digital Object Identifier (DOI®). “Just Accepted” is an optional service offered to authors. Therefore, the “Just Accepted” Web site may not include all articles that will be published in the journal. After a manuscript is technically edited and formatted, it will be removed from the “Just Accepted” Web site and published as an ASAP article. Note that technical editing may introduce minor changes to the manuscript text and/or graphics which could affect content, and all legal disclaimers and ethical guidelines that apply to the journal pertain. ACS cannot be held responsible for errors or consequences arising from the use of information contained in these “Just Accepted” manuscripts.



zation state with the global minimum energy along the structural relaxation process. R\*, I\* and P\* are all assumed to be the emissive states. The DFT optimized geometries of DPAC in R\*, I\* and P\* state are depicted. Note the difference in  $\Theta_b$  and  $\Theta_{S1}$ ,  $\Theta_{S2}$  among R\*, I\* and P\*.

As a result, at the early time domain (a few to few tens of ps) after Franck-Condon excitation, the temporal evolution of the emission of DPAC in the regular organic solvents reveals time-dependent panchromatic emission, consisting of initial charge transfer (R\*), intermediate (I\*) and the planarized, global minimized emission (P\*), which is drastically different from that of solely red emission (P\*) observed in the room-temperature steady state approach. The dynamics of structural relaxation of DHPs were affected by the steric hindrance raised by *N,N'*-disubstituted side chain motion. That is, the more steric hindrance induced by the bulky side chain may cause further retardation of structural relaxation along the planarization. This suggests the feasibility of “controlling” the planarization process through constraining the *N,N'*-disubstituted side chain motion.

### Scheme 1. The Synthetic Route and Chemical Structures of Chemically Locked 9,14-Diphenyl-9,14-dihydrodibenzo[*a,c*]phenazines DPAC-*n*<sup>a</sup>



<sup>a</sup> EDCI: 1-ethyl-3-(3-dimethylaminopropyl)carbodiimidehydrochloride, DMAP: 4-dimethylaminopyridine

Aiming to understand deeply the coupling of excited-state electronic processes with conformational motions, we thus conceived a series of annulated structures based on DPAC as a core, where *para* sites of the 9,14-diphenyl moieties are chemically threaded by dialkoxybenzene-alkyl-ester (or -ether) with different chain lengths, forming a series of new DHPs, DPAC-*n* (*n* = 1–8, see Scheme 1). Our aim was to impose various degrees of constraint to impede the excited-state structural deformation in hope of trapping a specific conformation so that we would be able to take a snapshot of the structural evolution and the associated photoluminescence. As elaborated in the following sections, the proof of concept is rendered by the constraint-dependent spectral evolution of DPAC-*n* spanning much of the panchromatic region. We also demonstrate that

scissoring the linkage leads to structural relaxation and consequently drastic changes of the emission property, demonstrating their fruitful potential in molecular sensing.

## 2. Results and Discussion

### 2.1 Design, Synthesis and Crystal structures.

A series of DPAC-*n* derivatives (*n* = 1–8, see Scheme 1), where *n* correlates with the different alkyl lengths, were synthesized and characterized. In a qualitative manner, we expected a decrease in constraint strength upon increasing *n*. As depicted in Scheme 1, treatment of DPAC with Vilsmeier reagent introduced two aldehyde groups in the *para* sites of 9,14-diphenyl of DPAC and gave the dialdehyde DPAC-CHO, which was subsequently reduced by sodium borohydride to give the key intermediate dibenzyl alcohol DPAC-OH, a structure that could be further cyclized by a dialkoxybenzene-alkyl-ether or -ester linkage with different chain lengths. Therefore, diol DPAC-OH reacted with Linker-1 1,2-bis(bromomethyl)benzene (NaH, THF, reflux) to deliver the smallest macrocycle DPAC-1 in this work. To tune the chain length, a series of compounds Linker-*n* (*n* = 2–8, see Scheme 1) end-capped with two carboxyl groups were prepared by nucleophilic substitution of 1,2-benzenediol with bromo-alkyl-acids bearing different alkyl chain lengths (see Scheme S1 in the supporting information (SI)). Finally, various macrocycles DPAC-*n* (*n* = 2–8) were obtained from esterification of diol DPAC-OH with Linker-*n* (*n* = 2–8) using EDCI/DMAP (see Scheme 1). Furthermore, the molecular structures of DPAC-*n* (*n* = 1, 3, 4 and 8) were further confirmed by single-crystal X-ray diffraction analysis.

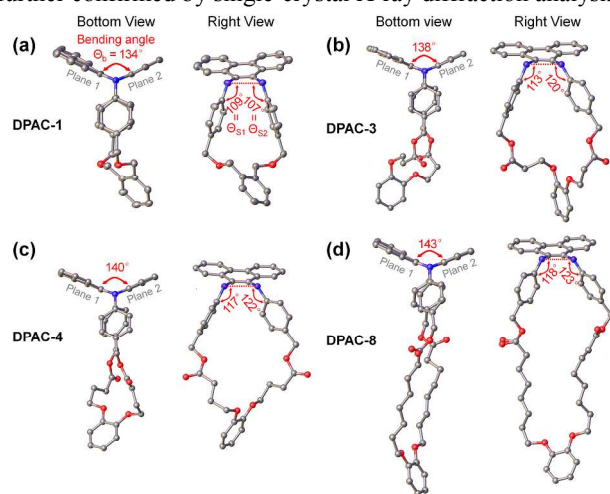


**Figure 2.** Single crystal structures of (a) DPAC-1, (b) DPAC-3, (c) DPAC-4 and (d) DPAC-8 from their two angles of view with the values of  $\Theta_b$ ,  $\Theta_{S1}$  and  $\Theta_{S2}$ .

By slow evaporation from dichloromethane/ethanol mixture solutions, we were able to grow single crystals of DPAC-*n* (*n* = 1, 3, 4 and 8). As shown in Figure 2, all corresponding X-ray structures reveal significant nonplanar distortions inherited from DPAC. For the convenience of analysis, three angles ( $\Theta_b$ ,  $\Theta_{S1}$  and  $\Theta_{S2}$ ) in the single-crystal structures were put forward and calculated. Using DPAC for illustration (see Figure 1a),  $\Theta_b$  ( $\angle C1-N1-N2-C2$ ) represents the bending angle between planes 1 (C1, N1 and N2) and 2 (N1, N2 and C2), while the angle between axes N1–N2 and N1–C3 or N2–C4 is denoted as  $\Theta_{S1}$  ( $\angle C3-N1-N2$ ) or  $\Theta_{S2}$  ( $\angle C4-N2-N1$ ). As a result,  $\Theta_b$  of 134° for DPAC-1 signifies the sharp decrease of the bent angle compared with those of DPAC-3, -4 and -8 (138–143°). In comparison to the  $\Theta_b$  of ~137° for DPAC, a decrease of up

to  $\sim 5^\circ$  in  $\Theta_b$  for **DPAC-1** may signify its further nonplanar distortion upon imposing the small alkyl chain constraint (vide infra). Meanwhile,  $\Theta_{S1}$  and  $\Theta_{S2}$  obviously rise from  $\sim 109^\circ$  to  $\sim 118^\circ$  and  $\sim 107^\circ$  to  $\sim 123^\circ$ , respectively. Note that in contrast to **DPAC**, the  $\Theta_{S1}$  of which is in close proximity to  $\Theta_{S2}$ , there is an obvious disparity between  $\Theta_{S1}$  and  $\Theta_{S2}$  in **DPAC-3**, **-4** and **-8**, which might be attributed to the flexible chain motion. Theoretically, upon electronic excitation of *N,N'*-disubstituted-dihydrobenzo[*a,c*]phenazines, a favorable bent-to-planar motion takes place to elongate the  $\pi$ -conjugation. In this sense, conformational information derived from single crystal analysis is consistent with the explanation, as structural strain decreases upon increase of the length of the alkyl chain.

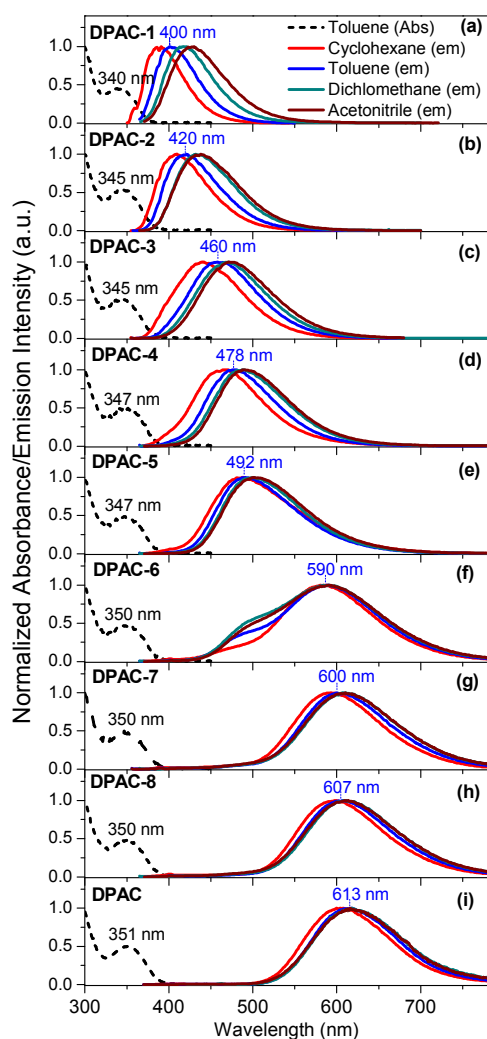


**Figure 3.** Steady-state absorption (in toluene, dashed line) and photoluminescence (solid line) spectra of **DPAC-1-8** (a) ~ (h) and **DPAC** (i) in various solvents at room temperature ( $\lambda_{ex} = 360$  nm).

**2.2 Steady State Photophysical Properties.** The normalized absorption and emission spectra of **DPAC-n** ( $n = 1\sim 8$ ) in various solvents from nonpolar cyclohexane to highly polar acetonitrile are shown in Figure 3 and Figure S1 (absorption in different solvents). The absorption peak wavelengths of 345-350 nm (onset at  $\sim 400$  nm) for **DPAC-2-8** in various studied solvents are about the same as that of **DPAC** (see Figure S1). In comparison, distinctly, both the absorption onset ( $\sim 385$  nm) and peak wavelength ( $\sim 340$  nm) of **DPAC-1** are slightly blue shifted by  $\sim 5$ -15 nm. On the one hand, this result indicates that

**DPAC-2-8** have a core chromophore similar to that of the constraint-free **DPAC** in the ground state. On the other hand, it also affirms the above structural analyses of a more crooked structure for **DPAC-1** (cf., **DPAC-2-8**), probably due to its tight structure constraint (vide supra, see Figure 2), rendering less  $\pi$ -delocalization.

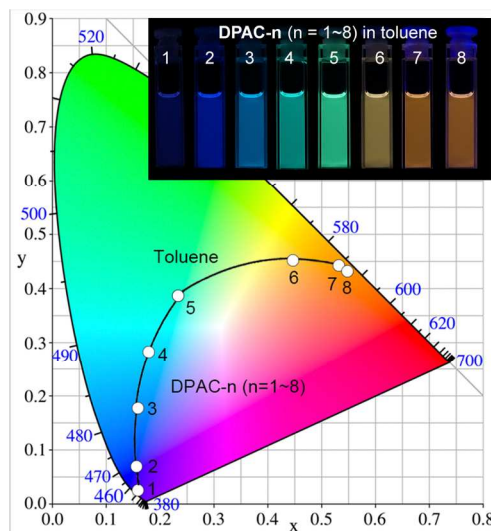


**Figure 4.** The chromaticity coordinates (CIE) of **DPAC-n** ( $n = 1\sim 8$ ) in toluene at room temperature. ( $\lambda_{ex} = 360$  nm). Insert: the fluorescence images of **DPAC-n** ( $n = 1\sim 8$ ) in toluene under irradiation of 365 nm UV light.

Despite the similarity in absorption spectra, **DPAC-n** exhibit remarkable differences in the emission properties. For **DPAC-1** and **DPAC-2**, the peak wavelength of fluorescence is located at 400 nm and 420 nm, respectively, in toluene (Figure 3a and b), followed by a trend of red shifted emission of **DPAC-3** (460 nm), **DPAC-4** (478 nm), **DPAC-5** (492 nm), **DPAC-6** (590 nm), **DPAC-7** (600 nm), and **DPAC-8** (607 nm) (Figure 3c-h). Accordingly, the emission peak wavelength is distinctly chain-length (i.e.,  $n$ ) dependent, being red shifted upon increasing  $n$  from 1 to 8. Corresponding to emission spectra, fluorescence images of **DPAC-n** ( $n = 1\sim 8$ ) clearly exhibit the red shift of emission with increment of chain-length (see Figure 4). From **DPAC-1** to **DPAC-8** in toluene, the emission color changes in an order of violet-blue (0.16, 0.03), palatinate blue (0.15, 0.07), maya blue (0.16, 0.18), turquoise (0.18, 0.28), aquamarine (0.23, 0.39), yellow (0.45, 0.45), orange (0.53, 0.44), and dark orange (0.55, 0.44). Apparently, the drastic chain-length dependent emission spans much of the visible range. For **DPAC-6**, in addition to the 590 nm emission, there appears to be another emission band maximized at  $\sim 490$  nm, showing dual or even multiple emission properties. Careful analysis also indicates that the blue and green emission for **DPAC-1-5** is dependent on solvent polarity, being red shifted as much as  $\sim 40$  nm in peak wavelength from cyclohexane to acetonitrile (Figure 3a-e), whereas the red emission for **DPAC-6-8** is only slightly dependent on solvent polarity (Figure 3f-h). This is also well demonstrated by the fluorescence images of **DPAC-n** ( $n = 1\sim 8$ ) in various solvents (see Figure S2). For **DPAC-4**, for example, with the solvent polarity increasing from nonpolar cyclohexane to highly polar acetonitrile, the emission color tunes from blue (0.17, 0.21) to green (0.21, 0.38), exhibiting remarkable solvatochromism. The results manifest the difference in the transition characters of these  $n$ -dependent, multiple color emissions with conformational motions.

It has been established that the nonplanar, V-shaped **DPAC** and its derivatives undergo structural bending motion between plane 1 and plane 2, i.e., along  $\Theta_b$  (see Figure 1b) in the electronically excited state, reaching a more planar configuration to extend the  $\pi$ -conjugation and hence an energy minimum.<sup>8a</sup> The bending process along  $\Theta_b$  is accompanied by the simultaneous optimization of  $\Theta_{S1}$  and  $\Theta_{S2}$  and hence encounters the steric hindrance introduced by the  $N,N'$ -disubstituted side-chains, which may evolve to a local minimum energy. As for the local minimum states, the nonplanar structure may localize the  $N,N'$ -disubstituents and dibenzo[*a,c*]phenazine moieties such that the transition possesses charge transfer character. Thus, previous time-resolved measurement was able to acquire various transient emissions at different time domains ascribed to initial charge transfer ( $R^*$ ), and intermediate ( $I^*$ ) and planarization ( $P^*$ ) emission (see Figure 1b).

In this study, via inserting an alkyl chain to impose the strain energy and halt the planarization midway, we were able to resolve different statuses of the structural evolution of the **DPAC** core chromophore even in a steady state manner, which is tentatively attributed to the initially prepared state emission (400-420 nm, **DPAC-1** and **DPAC-2**), the intermediate emission (460-520 nm, **DPAC-3-5**) and the planarization emission (600-620 nm, **DPAC-7** and **DPAC-8**). Despite the solvent independent absorption spectra, the short-wavelength emission bands (400-520 nm) are red shifted significantly upon increasing the solvent polarity, indicating their excited-state charge transfer property and hence the occurrence of solvatochromism. Conversely, the red emission band originating from planarized structure is much less subject to the solvent polarity, confirming its delocalized  $\pi\pi^*$  character.

To better understand the solvatochromism for short wavelength emissions of **DPAC-1-6**, the solvent effect on the emission properties can be further described by the Lippert-Mataga equation, which is and expressed as

$$\Delta\nu = \nu_{\text{abs}} - \nu_{\text{em}} = 2\Delta\mu^2\Delta f/(hca^3) + \text{constant}$$

where  $\Delta\nu$  denotes the Stokes shift,  $\nu_{\text{abs}}$  and  $\nu_{\text{em}}$  correspond to the absorption and the emission maxima in terms of wavenumbers ( $\text{cm}^{-1}$ ), respectively,  $\Delta\mu$  is the change of dipole moment between ground and excited states,  $h$  is Planck's constant,  $c$  is the speed of light,  $\Delta f$  is the orientational polarizability of the solvent, and  $a$  is the Onsager solvent cavity radius which is obtained by B3LYP/6-31+g(d,p) method in this study, assuming a spherical shape of the molecule. Figure S3 showcases the Lippert-Mataga plots of **DPAC-1-6**, and  $\Delta\mu$  is then calculated from the slope of the Lippert-Mataga plots and listed in Table S1. The deduced  $\Delta\mu$  values for **DPAC-1-6** in short-wavelength emission bands are large ( $> 7.7$  Debye), indicating that the  $R^*$  and  $I^*$  have a much larger dipolar moment than their corresponding ground states, confirming their excited-state charge transfer character. We also found that the  $\Delta\mu$  values for **DPAC-1-6** decrease upon increase of the length of the alkyl chain, due perhaps to the released constraint via the longer alkyl-ester linkage. Later we will elaborate that the intermediate corresponds to the skeleton motion of the side chain without significant planarization.

Upon planarization, the emission is dominated by the  $\pi\pi^*$  delocalized transition of dibenzo[*a,c*]phenazine moiety, which has a negligible charge transfer character. Interestingly, **DPAC-6** in the excited state reaches a critical stage where the intermediate emission decay rate is competitive with its rate of planarization, resulting in both intermediate and planarization

emissions. This viewpoint is firmly supported in the later time-resolved approach. Finally, independent of **DPAC-1-8**, normal Stokes shifted blue ( $\sim 400$ -430 nm) emission was observed for all titled compounds in solid (see Figure S4). The result firmly supports that the planarization process of **DPAC-1-8** required large-amplitude structural deformation, which is prohibited in solid due to the lattice constraint.

**2.3 Time Resolved Emission Spectroscopy.** To gain in-depth insight into the underlying relaxation mechanism, we then further performed time-resolved measurement. Two representative compounds, **DPAC-5** and **DPAC-6**, will receive particular focus. **DPAC-6** is of prime concern due to its obvious two emissions maximized at 490 and 590 nm, which possibly originate from intermediate and planarization emission, respectively. **DPAC-5** is selected as the other prototype because it has a proximal alkyl chain length with respect to **DPAC-6** but exhibits a very different emission spectrum.

As for **DPAC-5**, we first carried out a femtosecond fluorescence up-conversion study in toluene to probe the reaction dynamics in the early time domain. The results are shown in Figure 5a, and pertinent data are listed in Table 1. Upon 370 nm excitation and monitoring at the blue side of the emission (450 nm), the relaxation dynamics for **DPAC-5** exhibited an instant rise ( $<$  system response of 120 fs), followed by a very fast decay component of  $23 \pm 2$  ps decay components. Upon monitoring at 500 nm, 550 nm, 600 nm, and 650 nm, shown in Figure 5a, a finite rise component (negative pre-exponential value) gradually appeared, which was fitted to be within  $23 \pm 2$  ps. Also, independent of the monitored emission wavelength, there existed a very long population decay component that could not be completely acquired by the up-conversion technique. Alternatively, the long population decay kinetics was resolved by the pico-nanosecond time correlated single photon counting (TCSPC) measurement. The results depicted in Figure 5b reveal a single exponential decay component of 10.2 ns for all monitored emission wavelengths, indicating only a single population decay component.

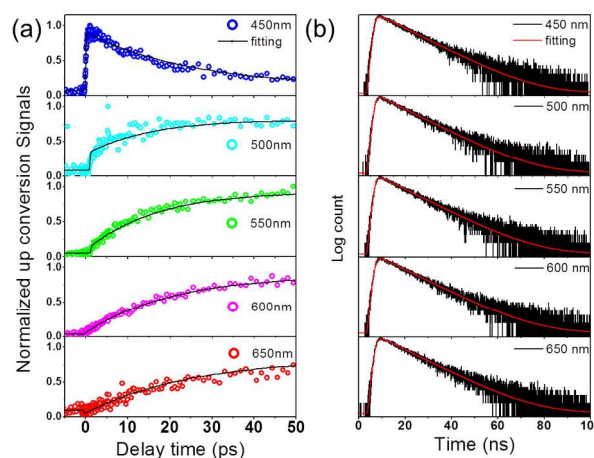


**Figure 5.** (a) Femtosecond and (b) nanosecond fluorescence transients of **DPAC-5** in toluene at room temperature observed at various wavelengths as depicted. See Table 1 for the fitting results. ( $\lambda_{\text{ex}} = 370$  nm). Note: For clarity, a logarithm plot is used in (b).

**Table 1. Fitting Results of TCSPC and Femtosecond Fluorescence Up-conversion Measurements for DPAC-5 and DPAC-6 in Toluene at Room Temperature**

$\lambda_{\text{probe}}$ (nm)	DPAC-5		DPAC-6	
	$\tau_{\text{obs}}$ (ns) <sup>a</sup>	$\tau_{\text{obs}}$ (pre-exp. factor) <sup>b,c,d</sup>	$\tau_{\text{obs}}$ (ns) (pre-exp. factor) <sup>a,c</sup>	$\tau_{\text{obs}}$ (pre-exp. factor) <sup>b,c,d</sup>
450	$\tau$ : 10.0	$\tau_1$ : 25 ps (0.94); $\tau_p$ : 10.2 ns (0.06) <sup>d</sup>	$\tau_1$ : 0.33 (0.89), $\tau_2$ : 9.01 (0.11)	$\tau_1$ : 17 ps (0.978); $\tau_2$ : 330 ps (0.007) <sup>d</sup> ; $\tau_p$ : 9 ns (0.015) <sup>d</sup>
500	$\tau$ : 10.7	$\tau_1$ : 17 ps (-0.40); $\tau_p$ : 10.2 ns (0.60) <sup>d</sup>	$\tau_1$ : 0.33 (0.84), $\tau_2$ : 9.15 (0.16)	$\tau_1$ : 9 ps (-0.310); $\tau_2$ : 330 ps (0.590) <sup>d</sup> ; $\tau_p$ : 9 ns (0.100) <sup>d</sup>
550	$\tau$ : 10.2	$\tau_1$ : 17 ps (-0.47); $\tau_p$ : 10.2 ns (0.53) <sup>d</sup>	$\tau_1$ : 0.33 (0.52), $\tau_2$ : 9.33 (0.48)	$\tau_1$ : 13 ps (-0.472); $\tau_2$ : 330 ps (0.526) <sup>d</sup> ; $\tau_p$ : 9 ns (0.002) <sup>d</sup>
600	$\tau$ : 10.3	$\tau_1$ : 20 ps (-0.42); $\tau_p$ : 10.2 ns (0.58) <sup>d</sup>	$\tau_1$ : 0.33 (-0.64), $\tau_2$ : 9.47 (0.36)	$\tau_1$ : 17 ps (-0.443); $\tau_2$ : 330 ps (-0.094) <sup>d</sup> ; $\tau_p$ : 9 ns (0.463) <sup>d</sup>
650	$\tau$ : 10.2	$\tau_1$ : 25 ps (-0.52); $\tau_p$ : 10.2 ns (0.48) <sup>d</sup>	$\tau_1$ : 0.33 (-0.62), $\tau_2$ : 9.61 (0.38)	$\tau_2$ : 330 ps (-0.460) <sup>d</sup> ; $\tau_p$ : 9 ns (0.540) <sup>d</sup>

<sup>a</sup> Lifetime was measured by using a TCSPC system with a pulsed hydrogen-filled lamp as the excitation source. ( $\lambda_{\text{ex}} = 370$  nm)

<sup>b</sup> Lifetime was measured by using an up-conversion system with femtosecond excitation pulses. ( $\lambda_{\text{ex}} = 370$  nm)

<sup>c</sup> Numbers in parenthesis are normalized pre-exponential factors of the decay in percentage.

<sup>d</sup> The time constant  $\tau_p$  was determined from the TCSPC result and used for the fitting of up-conversion signals.

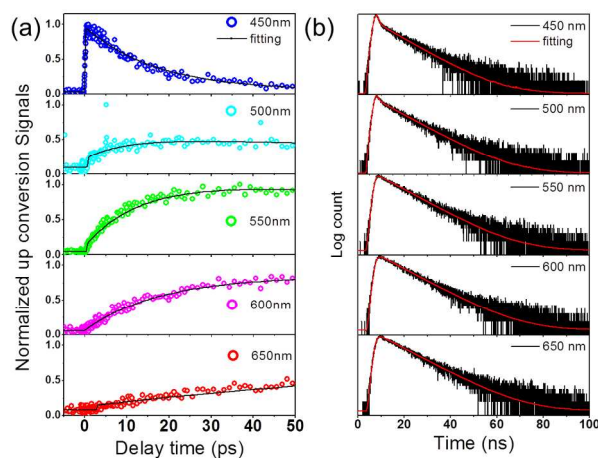


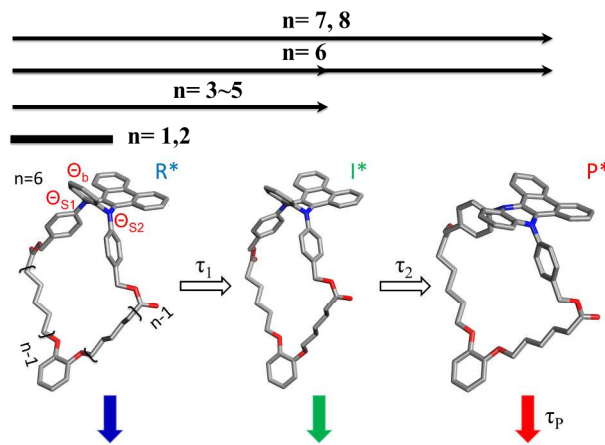
**Figure 6.** (a) Femtosecond and (b) nanosecond fluorescence transients of **DPAC-6** in toluene at room temperature observed at various wavelengths as depicted. See Table 1 for the fitting results. ( $\lambda_{\text{ex}} = 370$  nm). Note: A logarithm plot is used in (b) for clarity to show biexponential decay for 450 and 500 nm emissions.

In comparison to **DPAC-5**, much different relaxation dynamics were resolved for **DPAC-6**. Figure 6a reveals the early relaxation dynamics for **DPAC-6** in toluene, and pertinent fitted data are listed in Table 1. The relaxation dynamics at the blue edge of emission (450 nm) consisted of an instant rise (< 120 fs), followed by a fast decay of 17 ps and rather small amplitude, but much longer-lived, component that remained constant at the acquisition range of 50 ps. This long decay component was further probed by the nanosecond TCSPC. The result shown in Figure 6b (uppermost) revealed biexponential decay behavior with time constants fitted to be 0.33 ns and ~9 ns.

Upon increasing the monitored emission wavelengths to 500 nm and 550 nm, as shown in Figure 6a for femtosecond up-conversion data, the early 17 ps decay component observed at 450 nm disappeared and became a 17 ps rise component. Note that in Figure 6a (for 500 and 550 nm) the partial overlap between 17 ps rise and 17 ps decay components cancelled out, giving an instant rise component. Also, the long decay component increased the weighting ratio (% in pre-exponential factor) from 500 to 550 nm. The results of corresponding nanosecond TCSPC (see Figure 6b) also clearly indicated that the 0.33 ns decay component reduced its weighting ratio from

500 to 550 nm, which correlated with the appearance of a long rise component shown in the up-conversion study (see Figure 6b and Table 1). Extending the monitored wavelength to 650 nm, as shown in the TCSPC results (Figure 6b, lowermost), the 0.33 ns decay component was not resolvable anymore. Instead, a 0.33 ns rise component was resolved, followed by a ~9 ns population decay. This 0.33 ns long rise component can be seen from the up-conversion study as well (Figure 6a, lowermost), although the fluorescence up-converted data could not be precisely fitted due to the small acquisition time range of 50 ps.

### Scheme 2. The Proposed Excited-state Planarization Process of DPAC-n.<sup>a</sup>



<sup>a</sup> For  $\theta_b$ ,  $\theta_{S1}$  and  $\theta_{S2}$ , please see Figure 1b for DPAC.

The above time-resolved measurements clearly support the concept that the degree of excited-state planarization of **DPAC** can be controlled by chemically imposing an alkyl chain to act as a brake. As shown in Scheme 2, upon excitation at the lowest lying state ( $S_1$ ), **DPAC-5** undergoes a structural relaxation process from initially prepared state ( $R^*$ ) to an intermediate ( $I^*$ ), i.e.,  $R^* \rightarrow I^*$  with a time constant of  $23 \pm 2$  ps. The intermediate  $I^*$  is then subject to the strength imposed by the  $n = 5$  alkyl chain, such that further structural evolution is prohibited, resulting in a long population decay time of 10.2 ns. For **DPAC-6**, we reasonably assign the time constants of the  $R^* \rightarrow I^*$  and  $I^* \rightarrow P^*$  processes to be 17 ps ( $\tau_1$ ) and 0.33 ns ( $\tau_2$ ), respectively, followed by a population decay of the  $P^*$  state of ~9 ns ( $\tau_p$ ). Clearly, the  $R^* \rightarrow I^*$  processes for **DPAC-5** (24 ps) and **DPAC-6** (17 ps) are longer than that of **DPAC** (2.8 ps),

$\tau_1$ ),<sup>8a</sup> manifesting that the dialkoxybenzene-alkyl-ester linkages  $n = 5$  (**DPAC-5**) and  $n = 6$  (**DPAC-6**) increase the strain during the  $R^* \rightarrow I^*$  process. The increase in  $n$  releases strain and hence results in a faster  $R^* \rightarrow I^*$  process for **DPAC-6** than that for **DPAC-5**. The prohibition of the  $I^* \rightarrow P^*$  process for **DPAC-5** implies that the  $I^* \rightarrow P^*$  process requires a greater degree of motion, such that the strain introduced by the alkyl-ester linkage plays a more significant role (cf.  $R^* \rightarrow I^*$  process). This viewpoint is also supported by the  $I^* \rightarrow P^*$  process of 330 ps in **DPAC-6**, which is slower than that of 38 ps in **DPAC**<sup>8a</sup> by more than an order of magnitude. As a result, the intermediate emission **DPAC-6** in toluene can be clearly observed in a steady state manner.

We also performed the time-resolved measurement for **DPAC-1** and **DPAC-8**. **DPAC-1** was expected to impose the largest strain, as indicated indirectly by the smallest  $\Theta_b$  angle among the titled compounds (vide supra). Evidently, independent of the monitored emission wavelength (400-500 nm), solely a single emission decay of 2.0 ns was resolved, which is unambiguously ascribed to the population decay of the  $R^*$  state. Apparently, the  $R^* \rightarrow I^*$  process for **DPAC-1** is subject to the high energy barrier due to the strain imposed by the alkyl-ether chain. On the other hand, the time-resolved results shown in Figure S5 and Table S2 of SI for **DPAC-8** revealed nearly identical results with those of **DPAC**,<sup>8a</sup> indicating that the alkyl-ester chain of  $n = 8$  imposes negligible strain on the overall  $R^* \rightarrow I^* \rightarrow P^*$  process for **DPAC-8**.

**2.4 Computational Approaches.** We then developed theoretical support for the strain-imposed mechanism of this unique class of constrained V-shaped compounds. In this computational approach, we selected **DPAC-5** and **DPAC-6** as the prototypes and applied the time-dependent density functional theory (TD-DFT, see SI) to access the excited state properties, in which the  $S_0 \rightarrow S_1$  absorption was calculated directly from the Franck-Condon excitation of the geometry optimized ground state. Then the vertical  $S_1 \rightarrow S_0$  transition was calculated from the structurally optimized  $S_1$  state to obtain the emission energy gap. The calculated absorption and emission data are gathered in Table 2, including the experimental results in toluene for comparison.

For both **DPAC-5** and **DPAC-6**, as shown in Table 3, the calculated HOMOs are greatly localized in the center moiety *N,N'*-diphenyl-dihydropyrazine, while the LUMOs are all mainly localized at the fused phenanthrene ring. The results of computation clearly demonstrate that the lowest lying excited states for **DPAC-5** and **DPAC-6** are in part associated with the charge-transfer character (Table 3). We then computed the  $S_0 \rightarrow S_1$  transition for the other **DPAC-n** compounds and found that the HOMO/LUMO characters were all similar (see Table S3 and S4 of SI), which is also the same as that of **DPAC**.<sup>8a</sup> This, together with the negligible contribution of the alkyl-ether or alkyl-ester chain to the frontier orbitals, rationalizes similar absorption spectra for all the studied compounds.

We also performed the calculation of dipole moment for both ground (B3LYP/6-31+g(d,p) method) and first excited state (TD-B3LYP/6-31+g(d,p) method) based on their geometry optimized structures. As shown in Table S1, in a qualitative manner, the calculated large dipole moment for  $I^*$  in the  $S_1$  state for **DPAC-5** (22.0 Debye) and **DPAC-6** (24.5 Debye, see Table S1) versus the rather small dipole moment in  $S_0$  (6.6

Debye and 2.4 Debye for **DPAC-5** and **DPAC-6**, respectively) supports the excited-state charge transfer character. Unfortunately, the geometry optimized  $R^*$  cannot be located due to rather small  $R^* \rightarrow I^*$  energy barrier. We also calculated the vertical electronic transition from the ground state ( $R$ ), which is 384 nm and 390 nm for **DPAC-5** and **DPAC-6**, respectively. These values are similar to those calculated in other solvents such as in toluene (384 nm for **DPAC-5** and 390 nm for **DPAC-6**). In other words, the absorption spectrum is much less changed by the solvent polarity, reaffirming the occurrence of charge transfer in the excited state, followed by solvent relaxation and then planarization to account for the emission spectral changes.

At the ground state, both geometry optimized **DPAC-5** (Figure S6) and **DPAC-6** (Figure 7) have similar  $\Theta_b$  of  $136^\circ$ . The optimized ground state and corresponding Franck-Condon excited state are denoted as  $R$  and  $R^*$ , respectively. The vertical electronic transition from  $R \rightarrow R^*$  is calculated to be 384 nm for **DPAC-5** and 390 nm for **DPAC-6** in toluene (see Table 2). Note that the toluene environment was chosen because it has been widely exploited in the fluorescence up-conversion study. For **DPAC-5**, the computation result showed that in addition to  $R^*$ , there was only a global minimum in the  $S_1$  potential energy surface (PES) located at  $\Theta_b = 134^\circ$  (see Figure S6), which is denoted as  $I^*$  to correlate with the experimental result (vide supra). In stark contrast, and importantly, **DPAC-6** was found to have two energy minima, i.e., a local minimum at  $\Theta_b = 134^\circ$  denoted as  $I^*$  and a global minimum at  $\Theta_b = 158^\circ$  represented as  $P^*$  (Figure 7).

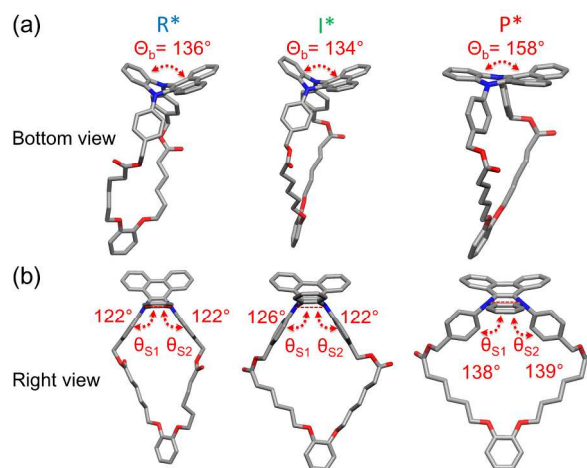


**Figure 7.** The (a)  $\Theta_b$  and (b)  $\Theta_{S1}$ ,  $\Theta_{S2}$  of the DFT optimized geometry of **DPAC-6** in the  $S_1$  excited state at the initially prepared state ( $R^*$ ), the local minimum ( $I^*$ ) and the global minimum ( $P^*$ ).

The vertical transition from  $I^* \rightarrow I$  for **DPAC-5** was calculated to be 492 nm, while the  $I^* \rightarrow I$  and  $P^* \rightarrow P$  transitions for **DPAC-6** were calculated to be 491 and 543 nm, respectively. The  $I^* \rightarrow I$  energy gap of  $\sim 490$  nm for **DPAC-5** and **DPAC-6** matches well the steady-state intermediate emission around 490 nm (see Figure 3), while the calculated 543 nm for the  $P^* \rightarrow P$  transition is consistent with the onset of freely planarized emission for e.g. **DPAC** (or **DPAC-8**) in toluene (see Figure 3).

**Table 2. The Experimental and Calculated Optical Characteristics for the DPAC-n Compounds<sup>a</sup>**

	Absorption $S_0 \rightarrow S_1$			Emission $S_1 \rightarrow S_0$			Stokes shift ( $\text{cm}^{-1}$ )		Q.Y.	$\tau_{\text{obs}}$ (ns) <sup>b</sup>
	$\lambda_{\text{exp}}$ (nm) ( $\epsilon/M^{-1}\text{cm}^{-1}$ )	$\lambda_{\text{calc}}$ (nm)	$f$	$\lambda_{\text{exp}}$ (nm)	$\lambda_{\text{calc}}$ (nm)	$f$	$\Delta E_{\text{exp}}$	$\Delta E_{\text{calc}}$		
DPAC-1	340 (6300)	375	0.0595	400	435	0.132	4411	3678	0.20	2.01
DPAC-2	345 (8600)	380	0.093	420			5175		0.43	4.64
DPAC-3	345 (14800)	382	0.1009	460			7246		0.59	7.53
DPAC-4	347 (11900)	387	0.1135	478			7898		0.54	8.95
DPAC-5	347 (10800)	384	0.1282	492	492	0.057	8493	5716	0.55	10.20
DPAC-6	350 (21200)	390	0.1332	490	491	0.048	8163	5274	0.34	0.33, 9.01 (450nm)
				590	543	0.068	11622	7224		0.33, 9.61(650nm)
DPAC-7	350 (5000)	389	0.1406	600			11904		0.24	8.18
DPAC-8	350 (5400)	390	0.1349	607			12097		0.26	8.32

<sup>a</sup> Data were recorded in toluene at room temperature.  $\lambda_{\text{exp}}$  = experimental absorption/emission wavelengths,  $\lambda_{\text{calc}}$  = calculated absorption/emission wavelengths,  $\epsilon$  = molar extinction coefficient,  $f$  = oscillator strengths,  $\Delta E_{\text{exp}}$  = experimental Stokes shift,  $\Delta E_{\text{calc}}$  = calculated Stokes shift, Q.Y. = emission, quantum yield. <sup>b</sup>  $\tau_{\text{obs}}$  = experimental emission lifetimes, which are measured by the time-correlated single photon counting (TCSPC, Edinburgh FL 900) method.

**Table 3. The Molecular Frontier Orbitals for DPAC-5 and DPAC-6 in Their Optimized Ground-state Geometries and the Relaxed Structures in the  $S_1$  Excited State at the Local Minima and Global Minima**

Bending Angle ( $\Theta_b$ )	DPAC-5		DPAC-6		
	136° (R and R*)	134° (I*)	136° (R and R*)	134° (I*)	158° (P*)
LUMO					
HOMO					

For fair comparison, we also attempted to locate the energy minimum of any optimized structure for **DPAC-1** in the excited state and found only one global minimum in the  $S_1$  state at  $\Theta_b = 134^\circ$ , which is the same as  $\Theta_b = 134^\circ$  for **DPAC-1** in the ground state. Therefore, we assign this state to be the optimized structure of the  $R^*$  state (in  $S_1$ ) reached by the Franck-Condon excitation. The estimated 435 nm emission for **DPAC-1** correlates well with its steady-state emission band maximized at 405 nm in toluene.

In addition to the difference in  $\Theta_b$  among  $R^*$ ,  $I^*$  and  $P^*$ , also noted is the changes of space/orientation on the  $N,N'$ -disubstituted side chain among the three states. For example, from an  $R^*$  state at  $\Theta_b = 136^\circ$  to the local minimum  $I^*$  at  $\Theta_b = 134^\circ$ , the results of calculation for **DPAC-6**, shown in Figure 7, indicate the conformational change at the  $N,N'$ -dialkoxybenzene-alkyl-ester (or ether) linkage via swinging and rotating round the  $N,N'$ -diaryls site, i.e., an increase of  $\Theta_{S1}/\Theta_{S2}$  from  $122^\circ/122^\circ$  to  $126^\circ/122^\circ$  and a decrease of  $\angle C5-C3-N1-N2$  from  $103^\circ$  to  $87^\circ$ . The results indicate that **DPAC-6**, along the structural relaxation, encounters steric

hindrance raised by the  $N,N'$ -disubstituted side chain. As for the  $I^* \rightarrow P^*$  process for **DPAC-6**, in addition to the changes in  $\Theta_b$  from  $134^\circ$  ( $I^*$ ) to  $158^\circ$  ( $P^*$ ), an increase of  $\Theta_{S1}/\Theta_{S2}$  from  $126^\circ/122^\circ$  to  $138^\circ/139^\circ$  and a decrease of  $\angle C5-C3-N1-N2$  from  $87^\circ$  to  $22^\circ$  were also obtained. Similar structural changes of the  $R^* \rightarrow I^*$  process were obtained for **DPAC-5**, evidenced by an increase of  $\Theta_{S1}/\Theta_{S2}$  from  $120^\circ/119^\circ$  to  $129^\circ/127^\circ$  and a decrease of  $\angle C5-C3-N1-N2$  from  $106^\circ$  to  $92^\circ$  (see Figure S6).

Apparently, the dynamics of structural relaxation should be affected by the  $N,N'$ -dialkoxybenzene-alkyl-ester (or ether) linkage. Unlike with **DPAC**, in addition to the steric hindrance of  $N,N'$ -dialkoxybenzene, the structure constraint imposed by the cyclic alkyl-ester chain (Scheme 1 and Figure 2) adds an additional barrier to hinder the planarization for **DPAC-1-6** and hence results in the distinct steady-state emission spectra and the corresponding relaxation dynamics (vide supra).

Due to the structural complexity, the computational approach to assess the activation energies along  $R^* \rightarrow I^*$  and  $I^* \rightarrow P^*$  PES for **DPAC-6** (also, **DPAC-7** and **DPAC-8**) unfor-

Unfortunately failed. Experimentally, due to the use of a rotating cell (clipped by two quartz plates) to contain the sample in the fluorescence up-conversion measurement, the temperature dependent study could not be performed. Alternatively, the much longer, sub-nanosecond  $I^* \rightarrow P^*$  process (vide supra) for **DPAC-6** made possible temperature-dependent study using the TCSPC technique. Accordingly, the experiment was performed in the temperature range of 283–243 K, where the viscosity of toluene varies only slightly (0.66–1.29 cp), to avoid environmental perturbation.<sup>9</sup> We then assumed that  $I^* \rightarrow P^*$  is the dominant decay for  $I^*$ , which follows the Arrhenius type of thermally activated process.

$$k_{obs} = Ae^{-E_a/RT}$$

where  $k_{obs}$  is the  $I^*$  emission decay rate constant, and  $A$  and  $E_a$  denote the frequency factor and activation energy of the  $I^* \rightarrow P^*$  planarization process. Accordingly, a logarithm of  $k_{obs}$  vs. the reciprocal of absolute temperature gave a straight line, and  $E_a$  and  $A$  were calculated to be 2.3 kcal/mol and  $1.59 \times 10^{11} \text{ s}^{-1}$ , respectively (see Figure 8). The relatively low frequency factor implies that the  $I^* \rightarrow P^*$  process is associated with a large amplitude motion, consistent with the appreciable changes of  $\Theta_b$  and  $\Theta_{S1}/\Theta_{S2}$  calculated along the planarization process.

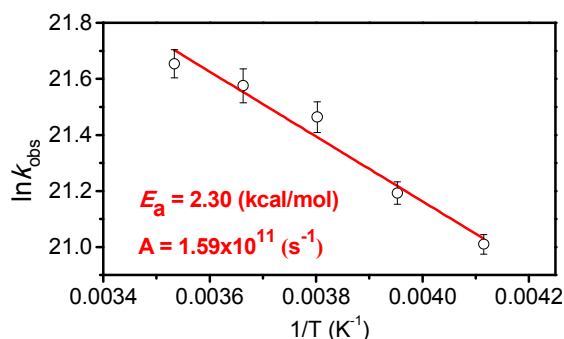
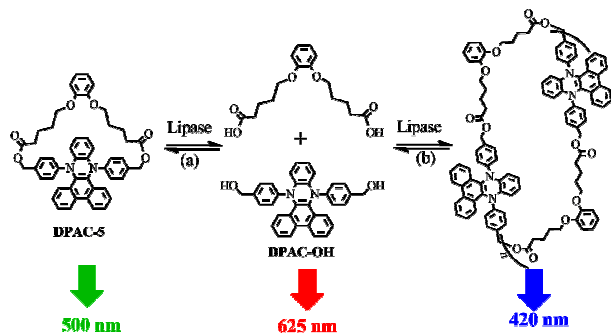


**Figure 8.** Arrhenius plot of the logarithm of rate constant ( $k_{obs}$ ) versus reciprocal of the absolute temperature of **DPAC-6** in toluene from 283 to 243 K.

**Scheme 3. (a) The Proposed Hydrolyzed Reaction of DPAC-5 by Triacylglycerol Lipase (3.1.1.3). (a)+(b) The Overall Possible Hydrolysis Mechanism Deduced from Experimental Results**



**2.5 Ring Opening and Its Potential Application.** As opposed to the imposition of constraint by the alkyl-ester linkages, releasing the structural freedom by severing the alkyl-ester linkages for **DPAC-2–6** should lead to drastic ratiometric changes of emission. We herein demonstrate a prototypical experiment for sensing triacylglycerol lipase (3.1.1.3) via its catalytic reaction to hydrolyze **DPAC-5**. Lipase is one of the most important industrial enzymes that catalyze the hydrolysis

or formation of lipids. It has been extensively exploited for catalytic chiral resolution because of the growing demand for enantiopure drugs.<sup>10</sup> The underlying mechanism of triacylglycerol lipase catalyzed **DPAC-5** hydrolysis and the associated signal transduction are illustrated in Scheme 3a.

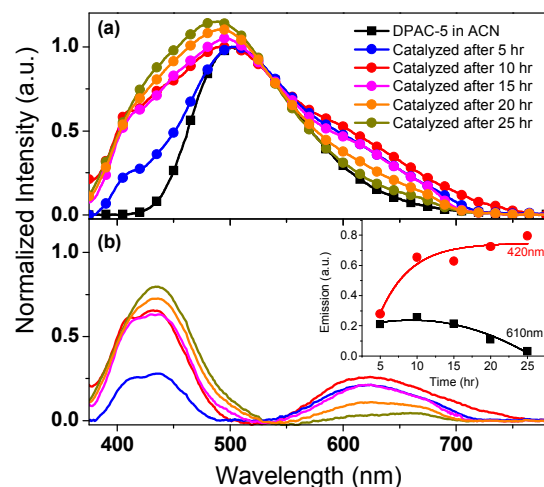


**Figure 9.** (a) The emission spectra of **DPAC-5** in acetonitrile (black solid square) and **DPAC-5** catalyzed by lipase with time (solid circles of various colors). (b) The difference in the emission spectra between **DPAC-5** in acetonitrile and after catalysis by lipase. ( $\lambda_{ex} = 360 \text{ nm}$ ). Inset: The time dependent intensity changes of 420 nm and 610 nm emission bands.

Theoretically, upon catalysis by lipase, the dual ester linkages of **DPAC-5** will be hydrolyzed, forming a **DPAC-OH** and a carboxylic acid (or carboxylate, depending on pH) product by rupturing the cyclic chain. Therefore, upon electronic excitation, planarization can take place for **DPAC-OH**, free from the constraint previously imposed by the alkyl-ester chain. The result should lead to drastic changes of the emission that can be exploited as an indicator of lipase activity. Experimentally, Figure 9a shows the emission spectra of **DPAC-5** in acetonitrile (ACN) and after catalysis by lipase with time in ACN:H<sub>2</sub>O = 99:1 (normalized to the same intensity of **DPAC-5** (peak wavelength) in ACN). The corresponding emission changed from a single 500 nm band to multiple emission bands. We then took the difference in these two emission spectra, and the resulting spectrum is shown in Figure 9b, in which two emission band maxima at 420 nm and 610 nm are observed, and the time-dependent intensity changes of these two emission bands are inserted in Figure 9b. While the 610 nm emission is unambiguously assigned to planarized  $P^*$  emission of **DPAC-OH**, the origin of the 420 nm emission band has to be further explored. We then performed a controlled experiment by hydrolyzing **DPAC-5** in a basic aqueous solution (pH = 11), followed by extraction of the hydrolyzed products by nonpolar solvents such as toluene or hexane. Lipase was then added to the products in nonpolar solvents. Due to the presence of trace water, the Le Chatelier principle drove the reaction mainly toward esterification. The emission spectra are shown in Figure S7 and Figure S8 of SI for n-hexane and toluene, respectively. Clearly, in addition to the minor 500 nm emission restored by the **DPAC-5** product, the 420 nm band is the dominant component, which may be ascribed to a cluster of esterification product from different assemblies (see Scheme 3 (a)+(b) processes). Consequently, the rigid internal environment of this cluster prohibits the

structural planarization, giving rise to the 420 nm emission ( $R^*$ ) from the initially prepared state.

### 3. Conclusion

In summary, we present a novel concept for modulating the excited-state process by systematically imposing various strengths of the constraint to the  $N,N'$ -disubstituted-dihydrodibenzo[*a,c*]phenazine donor-acceptor dyads **DPAC-n** ( $n = 1\sim 8$ ), in which  $n$  correlates with the alkyl length, such that the strength of the spatial constraint decreases as  $n$  increases, in an aim to harness the conformational flexibility. Among **DPAC-n**, the structures of **DPAC-1**, **DPAC-3**, **DPAC-4** and **DPAC-8** were identified by X-ray crystal analysis. In stark contrast to the large Stokes-shifted 610 nm red emission for **DPAC** (absorption onset  $\sim 400$  nm), drastic chain-length  $n$  dependent emission spanning from blue ( $n = 1, 2, \sim 400$  nm) and blue-green ( $n = 3\sim 5$ ) to green-red ( $n = 6$ ) and red ( $n = 7, 8, \sim 610$  nm) was observed and has been verified to originate from the charge transfer and planarization species, respectively. Scissoring the linkage releases the structural constraint and hence results in drastic changes of the emission; this approach was successfully exploited for sensing lipase activity using **DPAC-5**. The results thus demonstrate for the first time the systematic control of excited-state planarization of **DPAC-n**. Based on the formation and release of the constraint and hence the on and off of the planarization, future development of molecule machines driven by light may be feasible in  $N,N'$ -disubstituted-dihydrodibenzo[*a,c*]phenazines, which deserves much pursuit in both fundamental and applications.

### ASSOCIATED CONTENT

**Supporting Information.** Additional synthetic detail, crystallographic (including CIF), computational, and spectroscopic data along with complete references are provided. This material is available free of charge via the Internet at <http://pubs.acs.org>.

### AUTHOR INFORMATION

#### Corresponding Author

Email: [tianhe@ecust.edu.cn](mailto:tianhe@ecust.edu.cn) (H. Tian).

Email: [chop@ntu.edu.tw](mailto:chop@ntu.edu.tw) (P.-T. Chou).

#### Author Contributions

<sup>§</sup>These three authors made equal contributions.

#### Notes

The authors declare no competing financial interests.

### ACKNOWLEDGMENT

P.-T. Chou thanks the Ministry of Science and Technology, Taiwan, for financial support. H. Tian thanks National 973 Program (2013CB733700) and NSFC/China.

### REFERENCES

- (1) (a) He, G.; Guo, D.; He, C.; Zhang, X.; Zhao, X.; Duan, C., *Angew. Chem. Int. Ed* **2009**, *48*, 6132; (b) Zhang, X.; Rehm, S.; Safont-Sempere, M. M.; Würthner, F., *Nat Chem* **2009**, *1*, 623; (c) Mo, H.-W.; Tsuchiya, Y.; Geng, Y.; Sagawa, T.; Kikuchi, C.; Nakanotani, H.; Ito, F.; Adachi, C., *Adv. Funct. Mater.* **2016**, *26*, 6703-6710.
- (2) (a) Rotkiewicz, K.; Grellmann, K. H.; Grabowski, Z. R., *Chem. Phys. Lett.* **1973**, *19*, 315; (b) Birks, J. B., *Rep Prog Phys* **1975**, *38*, 903; (c) Rettig, W., *Angew Chem Int Edit* **1986**, *25*, 971; (d)

- Mataga, N.; Chosrowjan, H.; Taniguchi, S., *J Photoch Photobio C* **2005**, *6*, 37; (e) Cho, D. W.; Fujitsuka, M.; Choi, K. H.; Park, M. J.; Yoon, U. C.; Majima, T., *J Phys Chem B* **2006**, *110*, 4576.
- (3) Grabowski, Z. R.; Rotkiewicz, K.; Rettig, W., *Chem. Rev.* **2003**, *103*, 3899.
- (4) (a) Chien, Y. Y.; Wong, K. T.; Chou, P. T.; Cheng, Y. M., *Chem Commun* **2002**, 2874; (b) Terenzi, F.; Painelli, A.; Katan, C.; Charlot, M.; Blanchard-Desce, M., *J. Am. Chem. Soc* **2006**, *128*, 15742; (c) Wong, K. T.; Ku, S. Y.; Cheng, Y. M.; Lin, X. Y.; Hung, Y. Y.; Pu, S. C.; Chou, P. T.; Lee, G. H.; Peng, S. M., *J. Org. Chem.* **2006**, *71*, 456; (d) Liu, C.; Tang, K. C.; Zhang, H.; Pan, H. A.; Hua, J. L.; Li, B.; Chou, P. T., *J. Phys. Chem. A* **2012**, *116*, 12339.
- (5) (a) Demchenko, A. P.; Tang, K.-C.; Chou, P.-T., *Chem. Soc. Rev.* **2013**, *42*, 1379; (b) Padalkar, V. S.; Seki, S., *Chem. Soc. Rev.* **2016**, *45*, 169; (c) McDonald, L.; Wang, J.; Alexander, N.; Li, H.; Liu, T.; Pang, Y., *J. Phys. Chem. B* **2016**, *120*, 766.
- (6) (a) Clegg, R. M., *Curr. Opin. Biotechnol.* **1995**, *6*, 103; (b) Jia, X.; Chen, Q.; Yang, Y.; Tang, Y.; Wang, R.; Xu, Y.; Zhu, W.; Qian, X., *J. Am. Chem. Soc.* **2016**, *138*, 10778; (c) Sasmal, D. K.; Yadav, R.; Lu, H. P., *J. Am. Chem. Soc.* **2016**, *138*, 8789.
- (7) (a) Shukla, D.; Wan, P., *J. Am. Chem. Soc.* **1993**, *115*, 2990; (b) Vollmer, F.; Rettig, W.; Birckner, E., *J. Fluoresc.* **1994**, *4*, 65; (c) Doroshenko, A. O., *Theor. Exp. Chem.* **2002**, *38*, 135; (d) Chen, Y.; Zhao, J.; Guo, H.; Xie, L., *J. Org. Chem.* **2012**, *77*, 2192; (e) Yuan, C. X.; Saito, S.; Camacho, C.; Irle, S.; Hisaki, I.; Yamaguchi, S., *J. Am. Chem. Soc.* **2013**, *135*, 8842; (f) Yuan, C. X.; Saito, S.; Camacho, C.; Kowalczyk, T.; Irle, S.; Yamaguchi, S., *Chem-Eur J* **2014**, *20*, 2193; (g) Saito, S.; Nobusue, S.; Tsuzaka, E.; Yuan, C.; Mori, C.; Hara, M.; Seki, T.; Camacho, C.; Irle, S.; Yamaguchi, S., *Nat. Commun.* **2016**, *7*.
- (8) (a) Zhang, Z. Y.; Wu, Y. S.; Tang, K. C.; Chen, C. L.; Ho, J. W.; Su, J. H.; Tian, H.; Chou, P. T., *J. Am. Chem. Soc* **2015**, *137*, 8509; (b) Chen, J. W.; Wu, Y. S.; Wang, X. D.; Yu, Z. Y.; Tian, H.; Yao, J. N.; Fu, H. B., *Phys. Chem. Chem. Phys.* **2015**, *17*, 27658.
- (9) Assael, M. J.; Dalaouti, N. K.; Dymond, J. H., *Int. J. Thermo-phys.* **2000**, *21*, 291.
- (10) (a) Tang, L. H.; Xia, L. M.; Min, S.; Guo, H. Y., *Appl Biochem Biotech* **2007**, *142*, 194; (b) Kurtovic, I.; Marshall, S. N.; Zhao, X.; Simpson, B. K., *Fish Physiol Biochem* **2010**, *36*, 1041.

## Table of Contents artwork

